A novel partially open state of SHP2 points to a "multiple gear" regulation mechanism

Youqi Tao[1,‡], Jingfei Xie[2,3,‡], Qinglu Zhong[3,4,‡], Yongyao Wang[5,6,‡], Shengnan Zhang[2,3], Feng Luo[2,3], Fengcai Wen[7], Jingjing Xie[2,3], Jiawei Zhao[8], Xiaoou Sun[8], Houfang Long[2,3], Junfeng Ma[8], Qian Zhang[7], Jiangang Long[5], Xianyang Fang[8], Ying Lu[3,9], Dan Li[1], Ming Li[3,9], Jidong Zhu[2,3], Bo Sun[7], Guohui Li[3,4,*], Jiajie Diao[6,*], and Cong Liu[2,3,*]

From the [1]Bio-X Institutes, Key Laboratory for the Genetics of Developmental and Neuropsychiatric Disorders, Ministry of Education, Shanghai Jiao Tong University, Shanghai, China; [2]Interdisciplinary Research Center on Biology and Chemistry, Shanghai Institute of Organic Chemistry, Chinese Academy of Sciences, Shanghai, China; [3]University of the Chinese Academy of Sciences, Beijing, China; [4]Laboratory of Molecular Modeling and Design, State Key Laboratory of Molecular Reaction Dynamics, Dalian Institute of Chemical Physics, Chinese Academy of Sciences, Dalian, China; [5]Center for Mitochondrial Biology and Medicine, The Key Laboratory of Biomedical Information Engineering of Ministry of Education, School of Life Science and Technology, Xi'an Jiaotong University, Xi'an, China; [6]Department of Cancer Biology, University of Cincinnati College of Medicine, Cincinnati, Ohio, USA; [7]School of Life Science and Technology, ShanghaiTech University, Shanghai, China; [8]Beijing Advanced Innovation Center for Structural Biology, School of Life Sciences, Tsinghua University, Beijing, China; and [9]Beijing National Laboratory for Condensed Matter Physics and CAS Key Laboratory of Soft Matter Physics, Institute of Physics, Chinese Academy of Sciences, Beijing, China

Edited by Karen Fleming

The protein tyrosine phosphatase SHP2 mediates multiple signal transductions in various cellular pathways, controlled by a variety of upstream inputs. SHP2 dysregulation is causative of different types of cancers and developmental disorders, making it a promising drug target. However, how SHP2 is modulated by its different regulators remains largely unknown. Here, we use single-molecule fluorescence resonance energy transfer and molecular dynamics simulations to investigate this question. We identify a partially open, semiactive conformation of SHP2 that is intermediate between the known open and closed states. We further demonstrate a "multiple gear" regulatory mechanism, in which different activators (e.g., insulin receptor substrate-1 and CagA), oncogenic mutations (e.g., E76A), and allosteric inhibitors (e.g., SHP099) can shift the equilibrium of the three conformational states and regulate SHP2 activity to different levels. Our work reveals the essential role of the intermediate state in fine-tuning the activity of SHP2, which may provide new opportunities for drug development for relevant cancers.

SHP2 encoded by *PTPN11* is a nonreceptor protein tyrosine phosphatase, which plays a critical role in regulation of cellular processes and organ development (1, 2). As a member in SH2 family, SHP2 can be activated by a variety of upstream activators [e.g., insulin receptor substrate-1 (IRS-1), platelet-derived growth factor receptor, and IL-3 receptor] to mediate phosphotyrosine signaling networks, especially for the full activation of Ras/Erk pathway (3–5). Because the normal

function of SHP2 is essential for cell growth, proliferation, survival, and differentiation, dysregulation of SHP2 leads to numerous devastating human diseases such as juvenile myelomonocytic leukemias, Noonan syndrome, LEOPARD syndrome, and KRAS-driven cancers (6–10). In addition, SHP2 can be hyperactivated by CagA upon the infection of *Helicobacter pylori*, which causes gastric carcinogenesis (11, 12). The association of SHP2 with inhibitory receptors B and T lymphocyte attenuator, cytotoxic T lymphocyte-associated antigen 4, and programmed death 1 also makes SHP2 a promising target for cancer immunotherapy (13–15). Therefore, as the first reported oncogenic tyrosine phosphatase, SHP2 has long been regarded as an important target for cancer treatment. Numerous efforts have been conducted for the development of SHP2 inhibitors such as SHP099, 9ed, and JLR-2 (16–20).

SHP2 (1–593) contains four individual domains (21), including two tandem Src homology 2 (SH2) domains which recognize different upstream signaling activators, a C-terminal tail with two tyrosine phosphorylation sites and a central PTP catalytic domain for substrate dephosphorylation. The catalytic pocket on the PTP domain is formed by catalytic loops including P-loop, WPD-loop, K-loop, Q-loop, and pYr-loop for substrate binding, phosphoenzyme complex formation, and inorganic phosphate release (22–24). In the inactive state, SHP2 exhibits a self-inhibited conformation (17, 21, 25–27), in which the D'E-loop of the N-SH2 domain occupies the catalytic pocket of the PTP domain and blocks the access of substrates. Recently, two studies by using X-ray diffraction and NMR spectroscopy reported that the structure of the C-terminal truncated mutant SHP2 (E76 K, residues 1–525) adopted an open conformation with swiveling of the C-SH2 domain, moving of the N-SH2 domain across the entire body

---

of the PTP domain from one side to the other, and fully exposing of the PTP active site. Allosteric inhibitor SHP099 binding to SHP2 (E76 K) restored the closed conformation near-identical to WT [20, 28]. However, it remains unclear how SHP2 utilizes its tandem-SH2 domain to precisely respond to various upstream activators and subsequently control downstream signaling networks.

In this study, we utilize the single-molecule fluorescence resonance energy transfer (smFRET) approach [29, 30] to directly monitor the components and dynamics of the structural ensembles of WT and mutant SHP2 under different conditions. We find that SHP2 adopts three distinct conformational states in aqueous solution: an open state, a closed state, and a previously unidentified partially open state. We show that WT SHP2 is dominated in the closed state, while in contrast, the juvenile myelomonocytic leukemias–associated familial mutation E76A[31] dramatically reshapes the conformational landscape and dynamics toward the open and partially open states. By using the molecular dynamics (MD) simulation, we characterize the structure of the partially open state. We demonstrate that the activation of SHP2 by different endogenous and exogenous activators largely depends on the conformational preference to either the open or the partially open state. Thus, SHP2 dynamically switches its conformational equilibrium among inactive, semiactive, and active states to fulfill its distinct function in response to various regulators.

Results

Site-specific fluorescence labeling of SHP2 for smFRET measurement

Because the activation of SHP2 is triggered by the exposure of the catalytic pocket on the PTP domain, which is occupied by N-SH2 in the closed conformation [25], we envisioned a labeling pair for FRET with one in the N-SH2 domain and the other in the PTP domain. In this way, the relative movement between the N-SH2 and PTP domains can be directly captured by measuring the time-dependent changes in FRET efficiency [29, 30]. Accordingly, several labeling pairs with different distances were designed (Fig. 1A and Table S1). As for fluorophore attachment, the most commonly used cysteine-based strategy is not applicable [31] for SHP2, because SHP2 contains 10 cysteine residues globally distributed in the structure with C459 located at the center of the catalytic pocket. Alternatively, we employed a genetic code expansion technique whereby the stop codons (TAG) at labeling sites are used to code for an azido-modified unnatural amino acid azido-p-acetylphenylalanine (Azido-p-Phe), through an engineered tRNA/aminoacyl-tRNA synthetase system [32, 33] (Fig. 1A). For instance, WT full-length SHP2 (1–593) with two Azido-p-Phe incorporated at Q87/K266 (termed as Azido-WT-87/266) was expressed accompanied with two truncated variants because of the translation termination at the two mutated TAG sites (Fig. S1B). The fluorophores (Cy3 as FRET donor and Cy5 as FRET acceptor) were further conjugated to Azido-WT-87/266 *via* click reaction (termed as Fluor-WT-87/266), in which a protective regent Tris

(3-hydroxypropyltriazolylmethyl) amine was added to avoid oxidative damage of SHP2 and maintain the Cu (I) oxidation state [34, 35] (Fig. 1A).

The labeled SHP2 was immobilized on the standard PEGylated quartz surface *via* Fab-biotin and biotin-neutravidin interactions for smFRET study [36] (Fig. 1B). Control assays indicated that few molecules were detected by analysis tools (software smCamera, John Hopkins [31]) without Fab or protein, which confirmed that nonspecific fluorescence signals were prevented through this immobilization process (Fig. S1C). smFRET images of different SHP2 constructs including Fluor-WT-87/266, Fluor-E76A-87/266, Fluor-E76A-87/450, and Fluor-E76A-25/484 were acquired with a prism-based total internal reflection fluorescence (TIRF) microscope during donor excitation with a 532 nm laser (Figs. 1C and S1D). Donor-acceptor labeled molecules were identified with co-localization of the two fluorophores in both channels. Among SHP2 constructs, only the 87/266 pair exhibited relatively high fluorescence labeling efficiency with modest effect on impairment of the PTP activity of SHP2 upon introducing the Azido-p-Phe and dye-labeling (Fig. S1E). Therefore, we focused on the 87/266 labeling pair for the following smFRET studies of both WT and mutated SHP2.

Identification of a distinct partially open state between the open and closed states

We performed smFRET to investigate the conformational ensembles of SHP2 (WT) in aqueous solution. smFRET trajectories and the distribution histogram plotted from 208 individual recordings of molecules revealed that SHP2 (WT) is dominantly populated in a high FRET state ($\sim$0.70), corresponding to the closed state as seen in the crystal structure of SHP2 (WT) (Figs. 2A and S2). Intriguingly, in addition to a high FRET state, low-populated medium FRET and low FRET states were resolved. Because SHP2 (WT) exhibits basal PTP activity (Fig. S1E), the low FRET and medium FRET states with enlarged distances between the labeling pair may represent the active states of SHP2 where the N-SH2 domain is detached from the PTP domain thus to expose the catalytic pocket.

To further characterize the active states (low and medium FRET states) observed in the WT SHP2, we sought to examine the disease-related hyperactive mutant SHP2 (E76A) which exhibits much enhanced PTP activity compared with SHP2 (WT) [37] (Fig. S1E). We solved the crystal structure of full-length SHP2 (E76A) to a resolution of 2.5 Å by X-ray diffraction (PDB code: 6IHZ) (Fig. S3 and Table S2). The structure showed that SHP2 (E76A) retains a closed conformation in crystals which is nearly identical to that of SHP2 (WT) with overall root mean square deviation of 0.472 Å. However, small-angle X-ray scattering (SAXS) showed that SHP2 (E76A) features a more extended ensemble and dynamic conformation than that of SHP2 (WT) in aqueous solution, as evidenced by larger radius of gyration (R_g) and maximal end-to-end distance (D_{max}) in the pair distance distribution function and increased value at higher qR_g in the dimensionless

Kratky plots compared with WT (Fig. S4). Notably, the smFRET trajectories and the distribution histogram of SHP2 (E76A) reveal that it features a distinct conformational landscape with significantly populated medium (0.38) and low FRET (0.28) states compared with that of SHP2 (WT) in aqueous solution (Figs. 2B and S5). These results demonstrate that the E76A mutation unlocks the N-SH2 domain from the PTP domain and shifts the conformational equilibrium of SHP2 toward the more opened active states.

We next investigated the dynamic transition of SHP2 (WT) and SHP2 (E76A) between different states by Hidden Markov modeling analysis (31). As the real-time traces indicated, a large amount of SHP2 (E76A) molecules featured rapid and random conformational transitions between FRET states (Fig. S5). By calculating the fraction of traces with detectable dynamics and forming the transition-density plots (TDPs), we found that SHP2 (E76A) molecules featured a more dynamic conformational ensemble than that of SHP2 (WT) (Fig. 2). Moreover, the TDPs of SHP2 (E76A) show that the conformational transitions between the low and medium FRET states and those between the medium and high FRET states are much more frequent than the direct transition between low and high FRET states (Fig. 2B). These results suggest that the medium FRET states may represent an intermediate partially open state between the open (low FRET) state and the closed (high FRET) state.
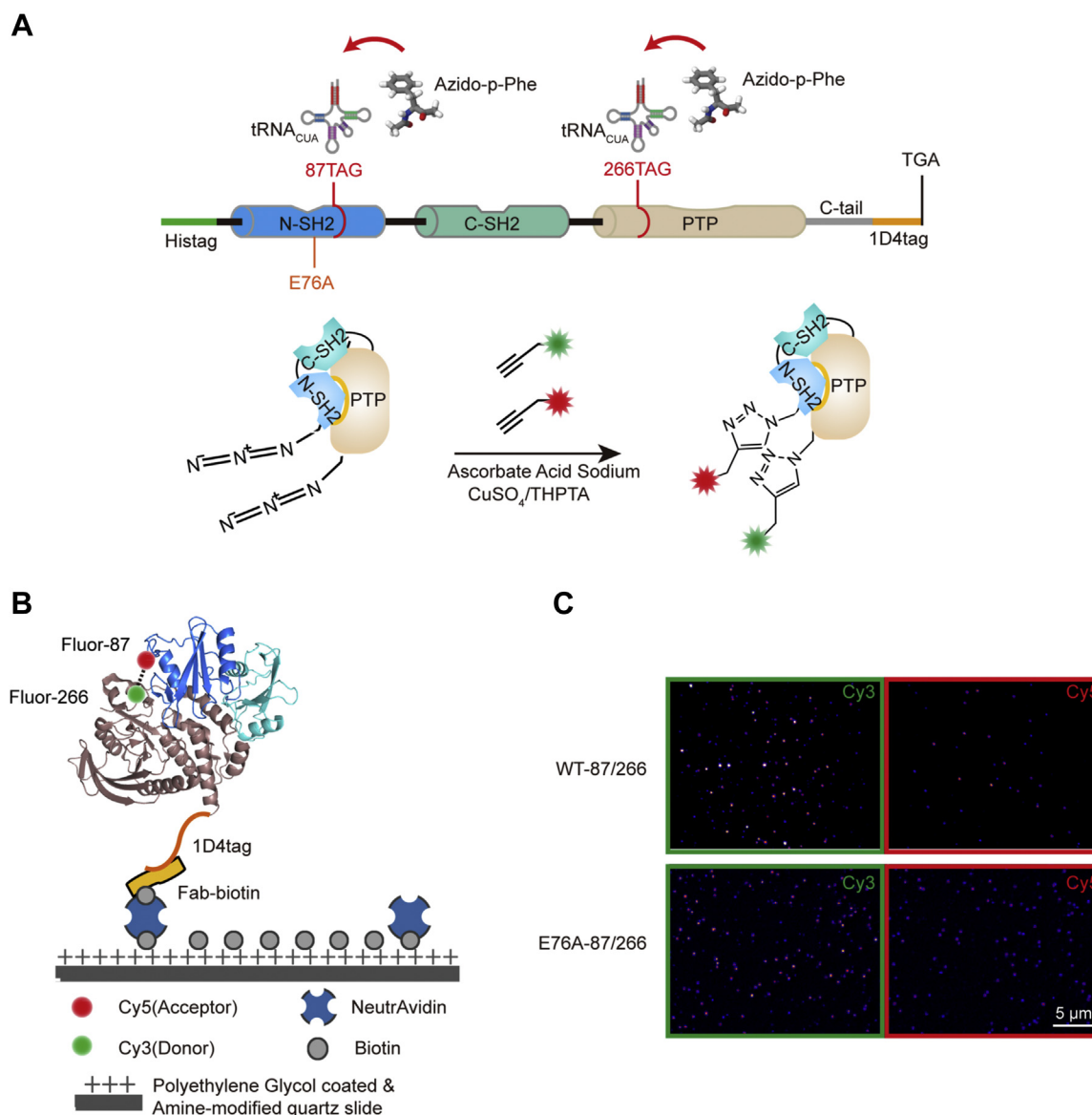

Figure 1. Strategy of the single-molecule FRET assay. *A,* strategy for site-specific incorporation of Azido-p-Phe into SHP2 at positions Q87/K266. The engineered tRNA/aminoacyl-tRNA synthetase system introduces the Azido-p-Phe through specially recognizing the stop codon TAG at 87/266. Alkyne-Cy3 and Alkyne-Cy5 were conjunct to azido through the click reaction, in which THPTA was added to protect protein from denaturing. *B,* schematic of protein immobilization for smFRET measurements. 1D4-tagged Fluor-SHP2-87/266 was immobilized on the surface of passivated quartz slide *via* Fab-biotin. *C,* representative smFRET images of Fluor-WT-87/266, Fluor-E76A-87/266 were acquired with a prism-based TIRF microscope during donor excitation with a 532 nm laser. THPTA, Tris (3-hydroxypropyltriazolylmethyl) amine; smFRET, single-molecule fluorescence resonance energy transfer.
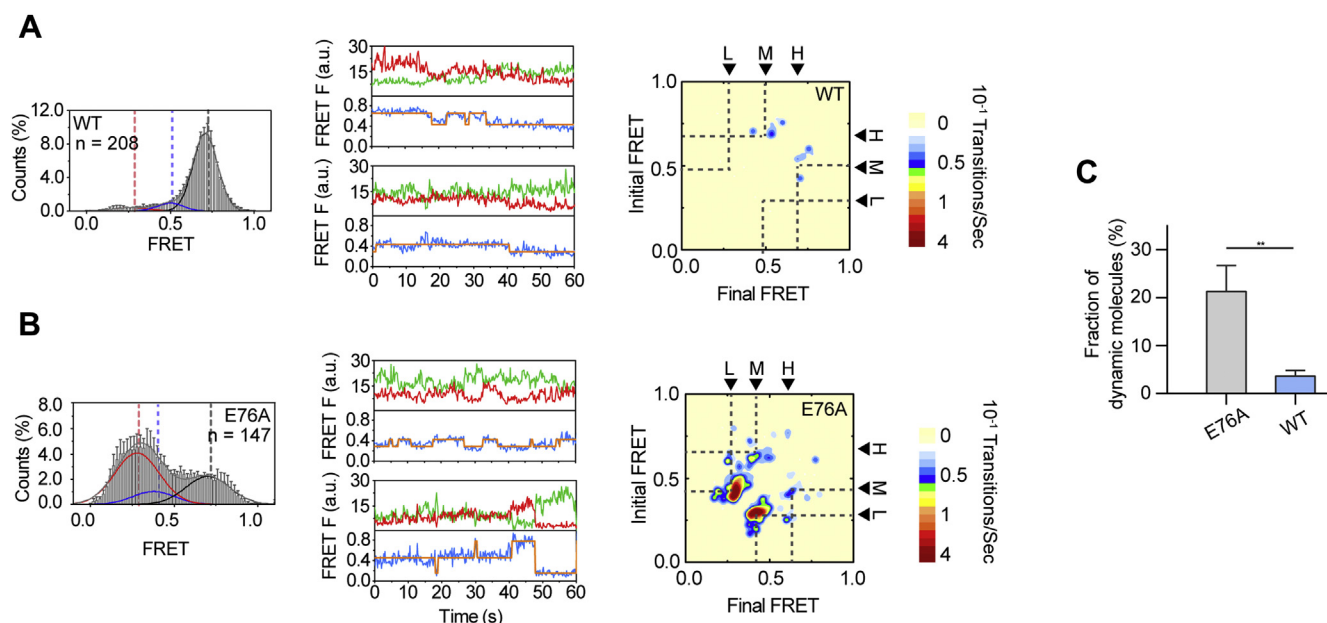
Figure 2. Single-molecule FRET assay reveals three conformational states of SHP2. *A,* (*Left*) FRET trajectories from individual WT-87/266 molecules were compiled into a population FRET histogram. *Error bars* are SEM. Decomposition of the FRET data resulted in three Gaussian curves representing the distribution of a low FRET state (*red*), medium FRET state (*blue*), and a high FRET state (*black*). *Dashed lines* indicate the distinct mean FRET values observed. The number (n) of smFRET traces compiled into each histogram is indicated. (*Middle*) real-time donor (*green*) and acceptor (*red*) intensity traces and FRET trace (*blue*) obtained from a single WT-87/266 molecule. Idealization of FRET trajectory (*orange*) was achieved by fitting to a three-state hidden Markov model. F, fluorescence; a.u., arbitrary units. (*Right*) TDPs for WT-87/266. Initial and final FRET (average FRET values before and after each transition respectively) were plotted as a two-dimensional chart between the three FRET states (*scale* at right). *B,* (*Left*) histogram of E76A-87/266. (*Middle*) representative smFRET trajectories for E76A-87/266 molecules. (*Right*) TDPs of E76A-87/266. *C,* the percentage of dynamic fractions of SHP2 WT and E76A. *Error bars* are SD, n = 3. Significance was determined by two-tailed *t* test. **$p < 0.002$. FRET, fluorescence resonance energy transfer; TDPs, transition-density plots.

Structural characterization of the partially open state revealed by MD simulation

To further verify the partially open state and its transition observed by smFRET, we modeled the conformational transition pathway from the closed state to open state by an enhanced sampling method of adiabatic biased molecular dynamics (ABMD) (38, 39). Derived free energy landscape in conformational space revealed three relatively stable conformations, supporting the existence of a partially open state in addition to the closed and open states (Fig. S6). The stationary distribution of the three states calculated by Markov state model revealed that SHP2 (WT) dominates in the closed state, whereas SHP2 (E76A) favors the partially open and open states (Fig. S6). Thus, the MD simulation results coincide with our observation in the smFRET studies and confirm the existence of the partially open state as an intermediate state between the close and open state of SHP2.

We next analyzed the structure of the partially open state of SHP2. From the structural cluster analysis of the partially open conformations, we found that the majority of the structural ensembles share a similar conformation where the N-SH2 rotates $\sim35°$ around the PTP domain derived from the closed state (Figs. 3A and S7A). Further structural analysis of the top three predominant partially open conformations (71% occupancy) reveals that the rotation of the N-SH2 domain flips up the D'E-loop and the F'A-loop (F71-A76) from deep inside of the catalytic pocket to the edge of the pocket (Figs. 3B and S7A). This conformational

translocation may disrupt the self-inhibition and increase the substrate accessibility to the catalytic pocket. However, the D'E-loop, F'A-loop, and the N'F-loop (N37-F41) of the N-SH2 domain located on the edge of the pocket can still form transient interaction with the catalytic loops of the PTP domain, which were observed in the subpopulation of the simulated partially open conformations.

Thus, we further assessed the interactions between the N-SH2 and the PTP domain in the simulated partially open conformations. We found that the N-SH2 domain of SHP2 (E76A) mainly interacts with the residues in the WPD-loop (including the residues both in the K-loop and WPD-loop, as the interaction with K-loop also restrict the motion of the WPD-loop (22, 24)), Q-loop, and P-loop (Fig. S8A). The interaction-based classification of SHP2 (E76A) revealed three predominant interaction patterns of the simulated partially open conformations (Fig. S8B). As shown in Figure 3, *C*−*E*, the residues T59, G60, D61, and Y63 in the D'E-loop of the N-SH2 domain form diverse interactions with the residues in the WPD-loop, the K-loop, the Q-loop, and the P-loop of the PTP domain. These interaction patterns are also conserved in the simulated partially open conformations of SHP2 (WT) (Fig. S7, *B*−*G*). Taken together, these results indicate that the partially open conformations release the D'E-loop of the N-SH2 domain from the self-inhibited conformation and relocate to the edge of the catalytic pocket, which may partially disturb the catalytic pocket and lead to the semiactivity of the PTP domain.
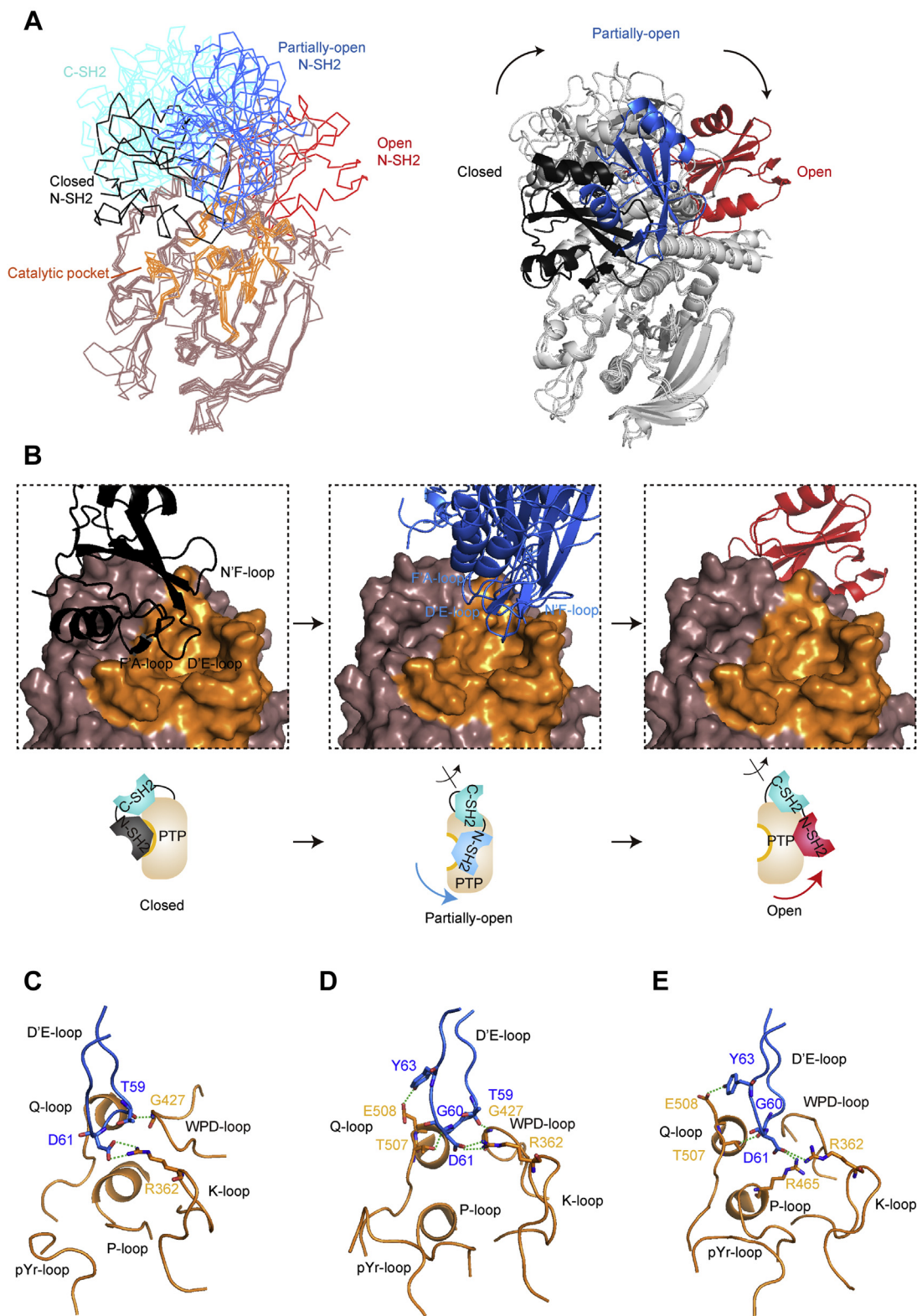
Figure 3. Structural detail of the partially open state of SHP2 (E76A) revealed by MD simulation. *A*, (*Left*) predominant partially open conformations from structural cluster analysis are superimposed. The N-SH2 domain of the open, partially open, and closed states are colored in *red*, *marine*, *black*, respectively. The C-SH2 domain, PTP domain, and the catalytic loops in all states are colored in *cyan*, *dirty violet*, and *orange*. (*Right*) representative conformations indicate the motion of the N-SH2 domain from closed state to partially open and open states. The N-SH2 domains in the closed, partially open, and open states are colored in *black*, *marine*, and *red*, the other domains in three states are colored in *gray*. *B*, (*Upper*) the zoom in reviews of the closed, open conformations, and the superimposing of the predominant partially open conformations from the cluster analysis highlight the local arrangement of the N-SH2 domain in three states. (*Bottom*) cartoons for the rearrangement of the N-SH2 domain in the closed, partially open, and closed states. *C–E*, the three most predominant partially open conformations from the interaction-based classification. The N-SH2, the PTP domain, and the catalytic loops are colored in *marine*, *dirty violet*, and *orange*, respectively. *C*, hydrogen bonds and salt bridges are built between the residues in the D'E-loop (*e.g.,* T59) and

Activators with monophosphorylated segments populate the partially open state of SHP2

We next asked whether and how SHP2 utilizes its partially open state to regulate its PTP activity. Previous studies showed that the PTP activity of SHP2 could be tightly regulated by a variety of upstream activators in diverse signaling transduction pathways (40–42). The SHP2 activators contain either a bis-phosphorylated (bis-P) segment binding to both N-SH2 and C-SH2 domains or a single monophosphorylated (mono-P) segment binding to the N-SH2 or C-SH2 domain of SHP2 with a relatively weaker activation effect (15, 40, 41). Thus, we performed smFRET to study whether SHP2 rearranges its conformational landscape (especially the partially open state) in response to different activators. We firstly examined a mono-P segment, EPIpYA-D, which is derived from an exogenous activator East Asian CagA in gastric carcinogenesis (43) (Fig. 4A). Intriguingly, titration of EPIpYA-D induced the conformational shift of both the closed and open states toward the medium FRET state, resulting in a predominant partially open state. As a control, the mono-P segment EPIpYA-C from Western CagA with much reduced ability for SHP2 (E76A) stimulation showed a minor effect on configuration redistribution of SHP2 (E76A) upon titration (Fig. 4, B and C). We further examined a third mono-P segment pY612 derived from an endogenous upstream activator IL-3 receptor (43, 44), which features similar stimulatory effect as EPIpYA-D (Fig. S9A). Consistently, pY612 remodeled the conformational distribution of SHP2 (E76A) to populate the medium FRET state (Fig. S9B). These results demonstrate that binding of the activator (mono-P segment) to a single SH2 domain may induce the shift of conformational equilibrium toward the partially open state.

Activators with bis-phosphorylated segments induce the open state and fully activates SHP2

We further examined how activators with bis-P segment affect the conformational equilibrium of SHP2 by using a bis-P segment pY1172-PEG$_8$-pY1222 derived from an endogenous activator IRS-1 (26, 45–47). We first split the bis-P segment pY1172-PEG$_8$-pY1222 into two mono-P segments pY1172 and pY1222. Previous studies demonstrated that pY1172 preferred to bind with N-SH2 domain over C-SH2 domain, whereas pY1222 showed preference for C-SH2 domain over N-SH2 domain (46). We titrated pY1172 and pY1222 to SHP2 (E76A) individually and found that either segment but not its dephosphorylated counterpart (1172 or 1222) (46) resulted in an increase of the population of the medium FRET state, which is similar to that observed from the mono-P segment EPIpYA-D and pY612 (Fig. 5, A and B and Fig. S10, A and B). This result indicates that the binding of mono-P to either the N-SH2 domain or C-SH2 domain is equivalent to alter the conformational distribution of SHP2 to a partially open state.

We next titrated the bis-P segment pY1172-PEG$_8$-pY1222 to SHP2 (E76A). The smFRET results showed substantial conformational shift toward the low FRET state in a dose-dependent manner (Figs. 5C and S11). During this process, the activator titration profile of the medium FRET state exhibits a bell-shaped curve with the peak at 5 nM activator. Because the binding of pY1172 to N-SH2 domain is 10-fold higher than the binding of pY1222 to C-SH2 domain (46), upon titration of bis-P segment, pY1172 may firstly bind to the N-SH2 domain and induce SHP2 to populate in the partially open state. As the concentration of bis-P segment further increases, pY1222 may sequentially bind to C-SH2 domain and cause transition of the partially open state to open state. Eventually, a sharp low FRET peak around ∼0.28 was formed at the saturated concentration of the activator. Switch between multiple conformational states may represent a way to regulate the efficiency of SHP2 activation depending on the concentration of the activators. As a control, the nonphosphorylated segment 1172-PEG$_8$-1222 which lacks the ability to activate SHP2 (46) showed a minimal effect on altering the conformational landscape of SHP2 (E76A) (Fig. S10C). This result demonstrated that the binding of the bis-P segment pY1172-PEG$_8$-pY1222 is effective to induce the open state of SHP2.

Moreover, we compared the PTP activity of SHP2 upon the mono-P and bis-P segments activation. The result showed that the two mono-P segments pY1172 and pY1222 which populate SHP2 in partially open state exhibited similar moderate effect in activating SHP2, whereas the bis-P dramatically boosted the PTP activity (Fig. 5, D and E). Therefore, this result confirms that the partially open state of SHP2 exhibits semiactivity. As we mixed equal molar of pY1172 and pY1222 to activate SHP2, the mono-P mixture showed a synergistic activation to SHP2 activity (Fig. S12A). Consistently, smFRET result showed that the conformational profile of SHP2 activated by the mixture of mono-P segments is more similar to that by the bis-P segment (Fig. S12B). These results indicate that as both N- and C-SH2 domains are bound with phosphorylated segments, SHP2 is able to be allosterically and synergistically turned on to the open, fully active state.

SHP099 interferes with the endogenous activator IRS-1 in reshaping SHP2 conformations

Next, we sought to assess the potential interference between activators and a potent allosteric inhibitor SHP099 (20) on reshaping the conformational landscape of SHP2. The results showed that in the presence of 125 nM pY1172-PEG$_8$-pY1222, at which SHP2 (E76A) was predominant in the open state, titration of SHP099 resulted in a conformational redistribution toward the closed state (Fig. S13A). However, this effect is significantly weakened compared with that untreated with pY1172-PEG$_8$-pY1222 (Fig. S13B). Conversely, titration of pY1172-PEG$_8$-pY1222 to SHP099 pretreated SHP2 (E76A), which was primarily locked in the closed state, can still unlock

---

WPD-loop (G427), K-loop (R362) which restrict the motion of WPD-loop. *D*, hydrogen bonds and salt bridges between the D'E-loop (*e.g.*, T59) and WPD-loop (G427), Q-loop (T507, E508), K-loop (R362) restrict the motion of WPD-loop and Q-loop. *E*, hydrogen bonds and salt bridges between the D'E-loop (*e.g.*, G60) and K-loop (R362), Q-loop (T507, E508), P-loop (R465) restrict the motion of WPD-loop, P-loop, and Q-loop. MD, molecular dynamics.
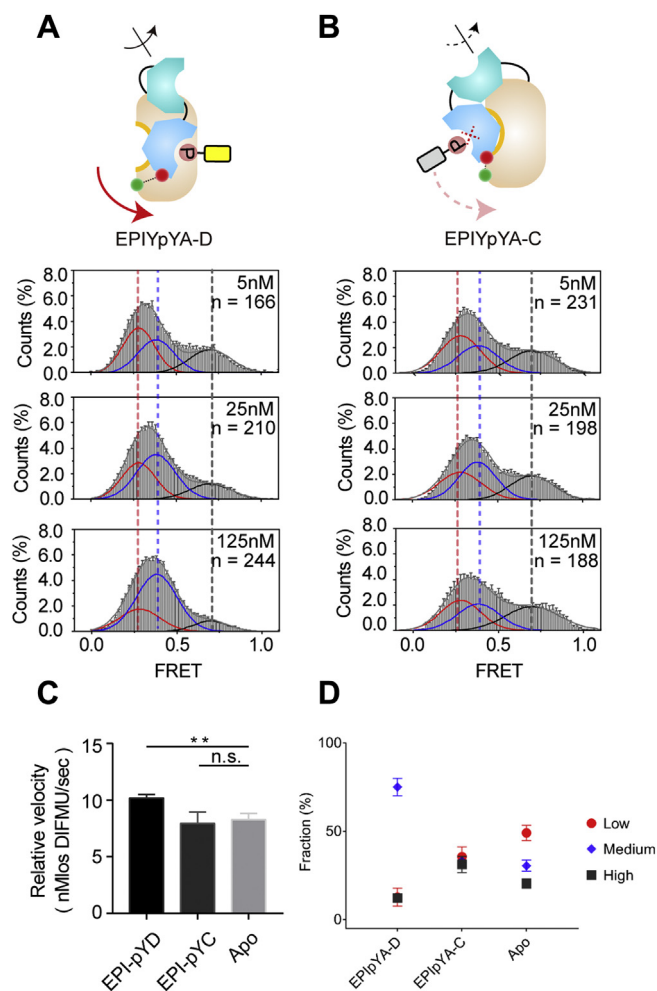
Figure 4. Different mono-P segments shift the conformational equilibrium of SHP2 toward the partially open state. *A,* (*Upper*) cartoon for binding of mono-P segment EPIpYA-D to the N-SH2 domain of SHP2. (*Bottom*) histograms for E76A-87/266 in the presence of different concentrations of EPIpYA-D. *B,* (*Upper*) cartoon for binding of mono-P segment EPIpYA-C to the N-SH2 domain of SHP2. The sequence between EPIpYA-C and the binding pocket of the N-SH2 domain is mismatched. (*Bottom*) histograms for E76A-87/266 in the presence of different concentrations of EPIpYA-C. *C,* PTP activity of Azido-E76A-87/266 and Azido-E76A-87/266 in the presence of 0.25 μM EPIpY-D and EPIpYA-C. Significance was determined by two-tailed *t* test. **p < 0.002 *Error bars* are SD, n = 3. *D,* fraction of three states in the presence of 125 nM EPIpYA-D and EPIpYA-C, *error bars* are SEM, n = 3.

the closed conformation gradually, but the efficiency was lower than that to the untreated SHP2 (Fig. S13, *C* and *D*). These smFRET data suggest that the inhibitory effect of SHP099 may be disturbed by the endogenous activators, which raises a concern of the effectiveness of the inhibitor in the biological circumstances.

Discussion

Recently, great progress has been made in single-molecule fluorescence-based structural biology. In comparison with X-ray crystallography and NMR spectroscopy, smFRET is superior to directly report on the heterogeneity and dynamics of biological macromolecules in different states without signals averaging (30, 48). In this work, smFRET enable us to directly monitor the heterogeneous ensemble of SHP2 in solution and

found a previously unidentified intermediate state with partially open conformation and semiactivity. By combining with MD simulation, we propose a "multiple-gear" regulatory mechanism underlying the regulation of SHP2 (Fig. 6), in which different activators prefer different conformational states of SHP2 to precisely adjust its PTP activity. For instance, allosteric activators that binds one (either N- or C-) SH2 domain may merely change SHP2 to the "low gear" with a partially open conformation and semiactivity; allosteric activators that simultaneously bind both N- and C-SH2 domains can synergistically change SHP2 to the "high gear" with a fully open conformation and maximal activity. Note that we cannot exclude the possibility that binding of mono-P segments to the N-SH2 or C-SH2 domain may result in different partially open states with minor structural difference, which cannot be distinguished by the current experimental settings. Binding to C-SH2 alone also leads to activation toward the intermediate state. We do not know the underlying mechanism yet. Further biophysical approach will help to reveal the fine regulation of SHP2 conformational states in multiple contexts.

The "multi-gear" model may help to understand the complexity of how various activators involved in different cellular signaling pathways to fine-tune the activity of SHP2, as hyperactivity or hypoactivity of SHP2 both may cause abnormal signaling transduction. In addition, this model may explain the strain-dependence bacterial virulence. As for the different strains of *H. pylori,* the East CagA (mono-P EPIpYA-D segment) and type II Western CagA (bis-P EPIpYA-C segment) but not typeIWestern CagA (mono-P EPIpYA-C segment) were reported to be risk factors of gastric cancer. Consistently, we showed that the mono-P segment EPIpYA-D but not the mono-P EPIpYA-C segment is efficient in inducing conformational redistribution and thus activating SHP2 (E76A). The type II Western CagA utilizes the tandem repeats of the EPIpYA-C as bis-P segment to elevate its stimulatory capability for SHP2. In contrast, the East Asian CagA with mono-P EPIpYA-D rarely duplicates (49, 50).

Our work demonstrated that the oncogenic mutations, allosteric inhibitors, and endogenous and exogenous activators can shift the equilibrium among the closed/inactive, partially open/semiactive, and open/fully active structural states of SHP2 (Fig. 6). This observation may inspire therapeutic drug development through retrieving the conformational profile of SHP2. In addition, the interference between activator and allosteric inhibitor explains the resistant of cell lines that express hyperactive SHP2 mutants to SHP099 (10, 20), which is probably because of the stimulatory effect of activators existed in cells. Thus, induction of the open/partially open states of SHP2 by the endogenous or exogenous activators in cells needs be considered in the potential drug development.

The dynamic equilibrium between the states of phosphatase-mediated dephosphorylation and kinase-mediated phosphorylation is central in different signaling pathways, where the SH2 domain serves as a major protein interaction module (51). In addition to SHP2, over 100 proteins were identified to contain SH2 domains, a significant amount of which of are consist of tandem-SH2 domain like
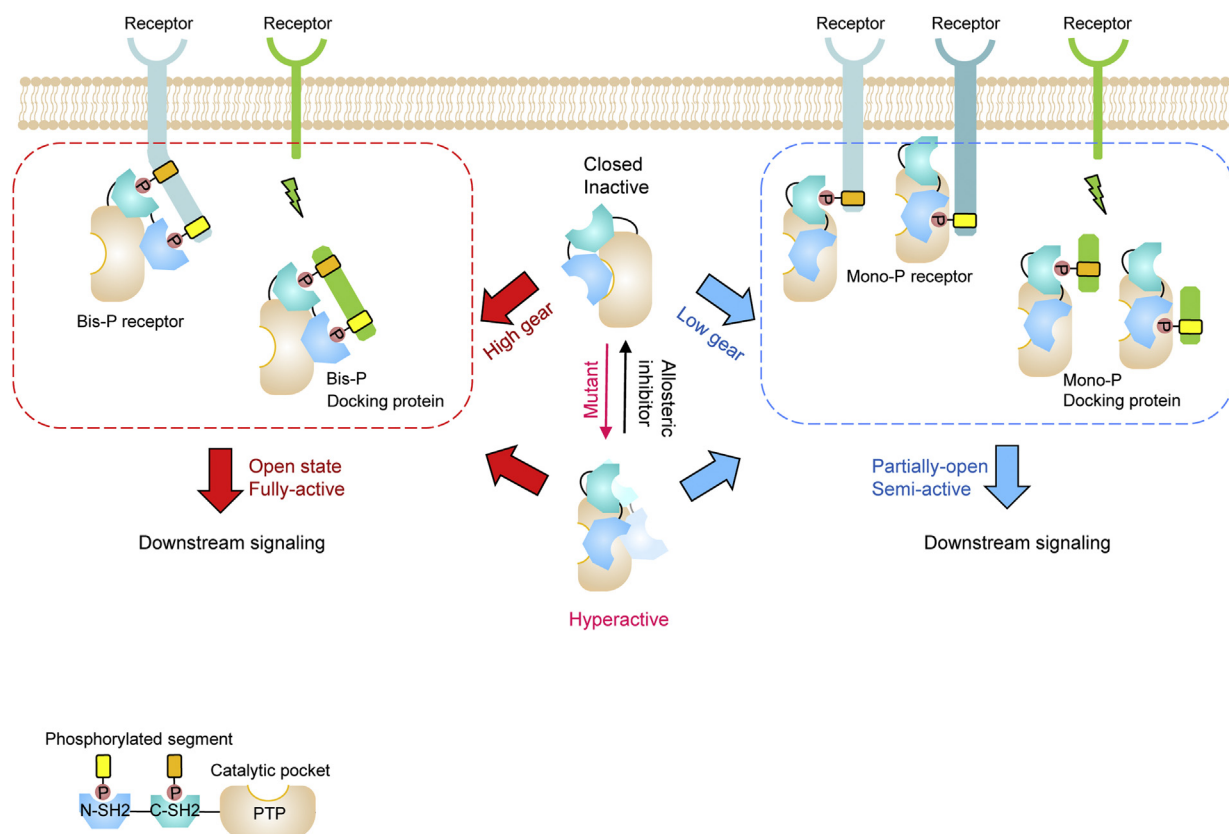
Figure 5. Conformational rearrangement in E76A-87/266 triggered by the bis-P segment pY1172-PEG$_8$-pY1222. *A* and *B*, (*Upper*) the cartoon for binding of mono-P segment pY1172 (a) and pY1222 (b) to SHP2. (*Middle*) histograms for E76A-87/266 in the presence of varying concentrations of pY1172 (a) and pY1222 (b). (*Bottom*) representative smFRET trajectories reveal transitions from low or high to medium FRET states in the presence of pY1172 (a) and pY1222 (b). *C*, (*Upper*) the cartoon for binding of the bis-P segment to SHP2. (*Middle*) histograms for E76A-87/266 in the presence of varying concentrations of pY1172-PEG$_8$-pY1222. (*Bottom*) a representative smFRET trajectory shows transitions from high to low FRET state through a medium FRET state in the presence of pY1172-PEG$_8$-pY1222. *D*, fraction of three states in the presence of 125 nM pY1172, pY1222 and pY1172-PEG8-pY1222. Error bars are SEM, n = 3. *E*, The PTP activity of apo Azido-E76A-87/266 and Azido-E76A-87/266 in the presence of 0.25 μM pY1172-PEG$_8$-pY1222, pY1172, and pY1222, respectively. Significance was determined by two-tailed *t* test. *Error bars* are SD, n = 3. smFRET, single-molecule fluorescence resonance energy transfer.

Figure 6. A "multi-gear" model for the regulation of SHP2 activity. The diagram represents the regulation of SHP2 by oncogenic mutations, allosteric inhibitors, and different activators. The binding of mono-P segment from receptors or docking proteins to a single (either N- or C-) SH2 domain switches SHP2 to the "low gear", which semiactivates SHP2 with dominant partially open conformations. While, binding of bis-P segment to both SH2 domains can switch SHP2 to the "high gear", which fully activates SHP2 with dominant open conformations. The oncogenic mutants can shift the conformational equilibrium of SHP2 from closed state to partially open and open states with hyperactivity, which can be retrieved by the addition of allosteric inhibitors.

SHP2 (52). Therefore, the "multi-gear" activation model derived from SHP2 study may represent a common mechanism in other tandem-SH2 domain containing proteins such as phosphatases (*e.g.,* other SHP proteins (53)), kinases (*e.g.,* spleen tyrosine kinase (54, 55), phosphoinositide 3-kinase (56–58)), and Ras guanosine triphosphatase (GTPase)-activating proteins (59, 60). In cell signaling network, the "multi-gear" mechanism combined with the specific selection of the SH2 domains may be generally involved in the recruiting and activating of tandem-SH2 domain containing proteins, subsequently determining which pathway(s) is activated downstream. And thus, the methods including smFRET with unnatural amino acids labeling and MD simulation used in this study may be applicable to reveal the dynamic structural transition and regulation of other tandem-SH2 domain containing proteins at the single-molecule level.

Experimental procedure

Plasmid construction

Human *PTPN11* cDNA encoding full-length (FL) SHP2 (1–593) were inserted into pET-28a bacterial expression vector. A flexible linker GSGS (GGCAGCGGCAGC) and a DNA fragment containing 1D4-tag sequence (ACCGAAACCAGC-CAGGTGGCGCCGGCG) at the 3'-terminus were inserted

into pET-28a by ClonExpress II One Step Cloning Kit (Vazyme biotech). Point mutations in SHP2 were introduced by site-directed mutagenesis. In SHP2 N-SH2 and PTP domains, V25, E83, Q87 and S264, K266, N336, M450, and V484 were substituted by TAG for the introduction of Azido-p-Phe. The original stop codon of this construct was also mutated from the amber stop codon to TGA.

Protein expression and purification

The procedures for expression and purification of SHP2 (WT) and SHP2 (E76A) are similar to those previously described. For expression of Azido-SHP2 (WT), the 87/266 mutant plasmid was co-transformed into BL21 (DE3) *Escherichia coli* with pEVOL-Azf. A single colony was picked up, inoculated into a 50 ml lysogeny broth culture with 1 mg/ml kanamycin and 0.3 mg/ml chloramphenicol, and allowed to grow overnight. After 14 h, 10 ml of the saturated culture was inoculated into 1 L of lysogeny broth with 1 mg/ml kanamycin and 0.3 mg/ml chloramphenicol and allowed to grow until the cells reached an OD_{600} value of 0.6 to 0.8, after which cells were allowed to overexpress proteins at 35 °C in the presence of 0.5 mM isopropyl β-D-1-thiogalactopyranoside (IPTG), 2% L-arabinose, and 0.242 mg/ml azido-p-acetylphenylalanine for 3 h. Then cells were pelleted at 4 °C and 4500 rpm for 20 min, resuspended in 45 ml of ice-cold 25 mM Tris (pH 8.0),

200 mM NaCl, 1 mM Tris-(2-carboxyethyl)-phosphine (TCEP), an EDTA-free protease inhibitor cocktail tablet (Roche Diagnostics), and lysed *via* sonication. The supernatant was loaded onto a HisTrap HP chelating column in 25 mM Tris-HCl, 200 mM NaCl, 2 mM TCEP. The protein was eluted in a gradient of imidazole. The protein was subsequently diluted to 50 mM NaCl with 20 mM Tris-HCl (pH 8.0), 1 mM TCEP, then applied to a HiTrap Q FastFlow column equilibrated with 20 mM Tris (pH 8.0), 50 mM NaCl, 1 mM TCEP. The protein was eluted in a gradient of NaCl. Fractions containing SHP2 were pooled and concentrated, then loaded onto a HiLoad Superdex200 PG 16/100 column, then buffer-exchanged into 50 mM Hepes (pH 7.5), 150 mM NaCl, and 0.5 mM TCEP. Azido-E76A-87/266 and other constructs (*e.g.,* Azido-E76A-87/450, Azido-E76A-87/336) with Azido incorporated followed the same procedures for expression and purification.

SAXS data collection and analysis

SAXS experiments were performed at beamline BL19U2 of National Center for Protein Science Shanghai at Shanghai Synchrotron Radiation Facility. The wavelength, λ, of X-ray radiation was set as 1.033 Å. Scattered X-ray intensities were collected using a Pilatus 1M detector (DECTRIS Ltd). The sample-to-detector distance was set such that the detecting range of momentum transfer [$q = 4\pi \sin\theta/\lambda$, where 2θ is the scattering angle] of SAXS experiments was 0.01 to 0.45 Å^{-1}. To reduce the radiation damage, a flow cell made of a cylindrical quartz capillary with a diameter of 1.5 mm and a wall of 10 µm was used. SAXS data were collected as 20 x 1 s exposures, and scattering profiles for the 20 passes were compared at 10 °C using 60 µl sample in 50 mM Hepes (pH 7.5), 75 mM KCl, 75 mM NaCl, 2 mM TCEP. Concentration series measurements for each protein sample were taken (1.17, 2.34, 4.68 mg/ml for WT, 1.67, 3.34, 6.68 mg/ml for E76A). The 2D images were reduced to 1D scattering profiles through azimuthally averaging after solid angle correction and then normalizing with the intensity of the transmitted X-ray beam, using the software package BioXTAS RAW. SAXS data processing, scaling, and calculations were conducted using the PRIMUS program of the ATSAS software suite. The buffer solution scatter curve was subtracted from the sample scatter to generate a background subtracted scatter curve. Linear Guinier plots in the Guinier region ($q*R_g< 1.3$) were confirmed in all experimental groups. Pair distance distribution functions of the particles P(r) and the maximum sizes D_{max} were computed using GNOM (5). The p(r)-derived radii of gyration were converted to real space values using GNOM.

Crystallization and structure determination of SHP2 (E76A)

The hanging drop vapor diffusion method was used for crystallization of SHP2 (E76A) (1–534) with the crystallization well containing 0.1 m Bicine pH 8.5, 15% w/v PEG 5000MME. 1 µl of SHP2 (E76A) was mixed with 2 µl of reservoir solution. Crystals were formed within 3 days and harvested, followed by cryoprotection using the crystallization solution with the addition of 20% glycerol, and flash-freezing by liquid nitrogen. Diffraction data were collected at BL19U1 beamline at Shanghai Synchrotron Radiation Facility. Data were processed using the XDS/XSCALE program.

Structure determination and refinements

Structure determination were performed by molecular replacement based on a structural model of SHP2 (PDB code: 6ATD) with all waters removed using the program Phaser. Crystallographic refinements were performed with the program PHENIX. Model building was performed with COOT. Data processing and refinement statistics are reported in Table S2.

Western blotting

The cells for expression of Azido-SHP2 (WT)-87/266 were induced at 35 °C for 3 h with four different conditions including (1) 0.5 mM IPTG, 0.242 mg/ml Azido-p-Phe, 2% L-Arabinose; (2), 0.242 mg/ml Azido-p-Phe, 2%; (3), 0.5 mM IPTG, 2% L-Arabinose; (4), 0.5 mM IPTG, 0.242 mg/ml Azido-p-Phe. Cells were then homogenized, and the cell lysate was resolved by SDS-PAGE and immunoblotted using specific antibodies (ProteinFind Anti-His Mouse Monoclonal Antibody, Transgen biotech).

Protein fluorescence labeling

SHP2 (E76A) and SHP2 (WT) with Azido-p-Phe at positions of 87/266 were concentrated to 5 µM in a labeling buffer containing 50 mM Hepes, 500 mM NaCl, and 0.1 mM TCEP, 5% glycerol, pH 7.5. A 1:1.2 mixture of Sulfo-alkyne-Cy3 (lumiprobe) and Sulfo-alkyne-Cy5 (lumiprobe) were added into the protein solution at protein/fluorophore ratio of 1:40. 1.5 mM Tris (3-hydroxypropyltriazolylmethyl) amine (Sigma) for protein protection and 300 µM CuSO$_4$ was added into the solution for click reaction. Labeling reactions were initiated with 4 mM sodium ascorbate and followed by incubation at 30 °C for 40 min. Free fluorophores were removed by a desalting column (Sephadex-G25, GE healthcare), and the labeled protein was eluted by elution buffer (50 mM Hepes, 500 mM NaCl, 0.5 mM TCEP, and 5% glycerol, pH 7.5). The calculated dual labeling efficiency for WT-87/266, and E76A-87/266 were 37.3 % and 39.9 %. SHP2 (E76A) with Azido-p-Phe at positions of 87/450, 25/484 followed the same procedures for labeling.

SHP2 phosphatase activity measurement

The PTP activity of SHP2 was monitored using the surrogate substrate 6,8-Difluoro-4-Methylumbelliferyl Phosphate (DiFMUP, Invitrogen) in a prompt fluorescence assay format. The phosphatase reactions were performed at room temperature in 96-well black polystyrene plate (flat bottom, low flange, nonbinding surface from Corning) with a final reaction volume of 100 µl. The reaction buffer includes 60 mM Hepes, pH 7.2, 75 mM NaCl, 75 mM KCl, 1 mM EDTA, and 2 mM TCEP. SHP2 (0.4 nM) was co-incubated with of various concentrations of pY1172-PEG$_8$-pY1222, pY1172, pY1222, 1172-PEG$_8$-1222, 1172, 1222, EPIpYA-D, EPIpYA-C, IL-3 receptor

pY612, respectively. After 10 min incubation at room temperature, DiFMUP was added to the reaction with a final concentration of 50 μM. Phosphatase activity was measured through the DiFMUP dephosphorylation on a microplate reader (SpectraMax i3) at 358 nm excitation and 450 nm emission. Raw velocity data were converted to product 6,8-difluoro-7-hydroxy-4-methylcoumari (DIFMU)/time. The sequences of the peptides used in this study are indicated in Table S3.

smFRET imaging with TIRF microscopy

Single-molecule FRET assays were performed as previously described. Slides were first coated with a mixture of 97% mPEG and 3% biotin-PEG, flow chambers were assembled using strips of double-sided tape and epoxy. Neutravidin and biotin-modified Fab-biotin (anti-1D4tag, a gift from Kobilka lab, Tsinghua University) were sequentially flowed into flow chamber, and each was incubated for 5 min in T50 buffer (50 mM KCl, 10 mM Tris-acetate, pH 7.5). Then, fluorescently labeled, 1D4-tagged SHP2 molecules were prepared in working buffer (50 mM Hepes, 500 mM NaCl, 2 mM TCEP, 5% glycerol, pH 7.5), immobilized on the PEGylated quartz surface after 10 min incubation. Subsequent smFRET imaging was conducted in imaging buffer (50 mM Hepes, 75 mM NaCl, 75 mM KCl, 0.5 mM TCEP, pH 7.5) containing an oxygen scavenging system consisting of 0.8 mg/ml glucose oxidase, 0.625% glucose, 3 mM Trolox, and 0.03 mg/ml catalase. For inhibitor or activators titration experiments, imaging was performed in the presence of increasing SHP099 and phosphorylated segments concentrations in imaging buffer and incubated for 10 min before image acquisition was started. All smFRET experiments were conducted at room temperature.

Single-molecule imaging was performed on a prism-type TIRF microscope equipped with a dual-laser excitation system (532 and 640 nm Crystal Laser) to excite Cy3 or Cy5. Fluorescence signals were collected by a water immersion objective lens and then passed through a notch filter to block out excitation beams. The emission signals from Cy3 and Cy5 were separated by a dichroic mirror and detected by the electron-multiplying charge-coupled device camera (iXon 897; Andor Technology). Data were recorded with a time resolution of 200 ms as a stream of imaging frames and analyzed with scripts written in interactive data language to give fluorescence intensity time trajectories of individual molecules.

Analysis of smFRET data

Preprocessing and analyses of single-channel current recordings were performed offline with smCamera software written in C++ (Microsoft) which was generously provided by Taekjip Ha (Johns Hopkins University). FRET efficiency, E, was calculated as $E_{FRET} = I_A/(I_A + I_D)$, in which I_A and I_D are the donor and acceptor intensity after background subtraction. Cy3 and Cy5 channel were mapped using tetraSpeck fluorescent microsphere beads (Invitrogen, 0.1 μM) by mapping tool in smCamera. Traces extracted from the movies were selected based on the following acceptance criteria: (1) no more than

one bleaching step for both donor and acceptor fluorophores; (2) traces showing a clear anticorrelated pattern; (3) lifetimes of both donor and acceptor fluorophore longer than 8s. All smFRET trajectories that met these criteria were used to calculate the apparent FRET efficiency and to generate population FRET histograms. Error bars in the histograms represent the SEM from at least three independent movies. The bin size of all histograms was set as 0.02. The final histograms were fitted to three Gaussian distributions performed with Origin Pro (Table S4). The complex smFRET trajectories were fit to a three-state based on hidden Markov modeling. To make sure real FRET transitions, all transitions were manually inspected based on anticorrelation of the donor and acceptor intensity signals. The idealized smFRET trajectories were further analyzed to calculate TDPs. The fraction of detectable dynamic traces was calculated from the idealized smFRET traces that exhibited at least one FRET transition and lasted at least two data points. All of the experiments were repeated at least three times, and no significant difference was found between these replicates.

Molecular dynamics simulation

The crystallographic coordinates of three structures SHP2 (WT, E76A and E76A+SHP099) in the closed state and one structure of SHP2 in the open state were used for MD simulation (PDB code: 4DGP, 5XZR, 5EHR and 6CRF). The missing residues in the four structures were completed using MOD-ELLER 9.17. The force field of SHP099 was generated using Antechamber module in AmberTools. Each of structures in the closed state was positioned into a 10 nm cubic box and dissolved with TIP3P waters. 0.15 M chloride and sodium ions were added to neutralize the net charge of the system. The system was subjected to energy minimization using the steepest descent algorithm, then gradually heated to 300 K under NVT ensemble and equilibrated under NPT ensemble. To seek a proper transition path from the closed state to the open state, the initial closed structure was simulated moving towards target open structure by ABMD. ABMD is an enhanced sampling method developed to connect any two points in the conformational space of a given system. Briefly, this method is based on the introduction of a biasing potential which is zero when the system is moving to the target point and which damps the fluctuations when the system is moving to the opposite. Consequently, ABMD simulation would coincide with the minimum free-energy path from the initial to the target conformation, on account of the biasing potential which does not exert work in directing the system towards a specific direction. Two hundred different intermediate conformations were homogeneously selected from the path mentioned above to sample conformational transitions. Production run of 200 ns was started with each intermediate conformation and repeated three times independently. Totally, for each of the three conditions, WT, E76A, and E76A in the presence of SHP099, 600 trajectories were calculated free energy landscape in conformational space. Then, three metastable conformational states were identified and assigned as

the closed, partially open, and open states. Stationary distribution of each metastable state was derived by Markov state model.

The principle of free energy estimating is as follows. Given a system evolving at fixed temperature, fixed number of particles, and fixed volume, it will explore different conformations with a probability, $p(q) \propto e^{-E(q)/k_B T}$, where q are the microscopic coordinates, E is the system energy, k_B is the Boltzmann constant, T is the system temperature. The probability can be recast to a free energy by taking its logarithm, $F(q) = -k_B T log p(q)$, after normalizing the free energy of conformations with the maximum probability to zero.

Thousands of conformations in the partially open state were selected from the trajectories after 150 ns for further analysis. Distribution of relative position between the N-SH2 and PTP domain was assessed by cluster analysis. Hydrogen bonds and salt bridges between N-SH2 and PTP domain were counted using VMD Software. The regions of the catalytic loops include P-loop (C459-R465), Q-loop (Q506-Q510), WPD-loop and K-loop (W423-S430&E361-K366), and pYr-loop (R278-N281). According to the classification by interactions between N-SH2 domain and the involved loops, the predominant residual interactions and representative conformations in the partially open state were validated and presented.

All MD simulations were performed using OpenMM 7.3 with ff14sb force field. Besides, enhanced sampling simulations were implemented with the PLUMED plug-in. The Andersen Thermostat was applied to couple temperature in the system with a collision frequency of 1.0 ps^{-1}. The Monte Carlo barostat was used to control pressure in the system at 1 bar. Particle-Mesh Ewald method was utilized to treat the electrostatic interactions with cutoff distance of 0.9 nm. The same cutoff value was chosen for treating the van der Waals interactions. The SETTLE algorithm was applied to keep TIP3P water rigid. The hydrogen of mass in protein and inhibitor was increased to 4 amu. The added mass was subtracted from the bonded heavy atom. Hence, the integration step size was set to 4 fs. To increase water diffusion rate, the mass of water oxygen was reduced to 2 amu. This change did not affect the thermodynamic equilibrium properties. Free energy and Markov state model analyses were achieved by pyEMMA software package.

Data availability

Coordinates and structure factors for the full-length SHP2 (E76A) are deposited in the protein data bank under PDB ID code 6IHZ. All other data are available from the corresponding authors upon reasonable request and/or are included with the manuscript (as figure source data or supporting information).

Supporting information—This article contains supporting information.

Author contributions—C. L., J. D., and G. L. designed the project. Y. T., J. X., and Y. W. performed the biochemical and smFRET experiments. Q. Z. and G. L. performed the MD simulation calculations. F. L. built and refined the structure model. J. M. and X. F. processed the SAXS data. All the authors are involved in analyzing the data and contributed to manuscript discussion and editing. D. L. and C. L. wrote the manuscript. Y. T., J. X., and C. L. revised the manuscript.

Conflict of interest—The authors declare that they have no conflicts of interest with the contents of this article.

Abbreviations—The abbreviations used are: ABMD, adiabatic biased molecular dynamics; DiFMUP, 6,8-Difluoro-4-Methylumbelliferyl Phosphate; IRS-1, insulin receptor substrate-1; MD, molecular dynamics; SAXS, small-angle X-ray scattering; smFRET, single-molecule fluorescence resonance energy transfer; TCEP, Tris-(2-carboxyethyl)-phosphine; TDP, transition-density plot; TIRF, total internal reflection fluorescence.

References

1. Neel, B. G., Gu, H., and Pao, L. (2003) The Shp'ing news: SH2 domain-containing tyrosine phosphatases in cell signaling. *Trends Biochem. Sci.* **28**, 284–293
2. Grossmann, K. S., Rosário, M., Birchmeier, C., and Birchmeier, W. (2010) Chapter 2 - the tyrosine phosphatase Shp2 in development and cancer. In Vande Woude, G. F., Klein, G., eds., *Advances in Cancer Research* **106**. Elsevier Academic Press, San Diego, CA: 53–89
3. Matozaki, T., Murata, Y., Saito, Y., Okazawa, H., and Ohnishi, H. (2009) Protein tyrosine phosphatase SHP-2: A proto-oncogene product that promotes Ras activation. *Cancer Sci.* **100**, 1786–1793
4. Shearer, W. T., Rosenwasser, L. J., Bochner, B. S., Martinez-Moczygemba, M., and Huston, D. P. (2003) Biology of common β receptor-signaling cytokines. *J. Allergy Clin. Immunol.* **112**, 653–665
5. Xu, D., and Qu, C.-K. (2008) Protein tyrosine phosphatases in the JAK/STAT pathway. *Front. Biosci.* **13**, 4925–4932
6. Östman, A., Hellberg, C., and Böhmer, F. D. (2006) Protein-tyrosine phosphatases and cancer. *Nat. Rev. Cancer* **6**, 307
7. Bentires-Alj, M., Paez, J. G., David, F. S., Keilhack, H., Halmos, B., Naoki, K., Maris, J. M., Richardson, A., Bardelli, A., Sugarbaker, D. J., Richards, W. G., Du, J., Girard, L., Minna, J. D., Loh, M. L., *et al.* (2004) Activating mutations of the Noonan syndrome-associated *SHP2/PTPN11* Gene in human solid Tumors and Adult Acute Myelogenous leukemia. *Cancer Res.* **64**, 8816–8820
8. Kontaridis, M. I., Swanson, K. D., David, F. S., Barford, D., and Neel, B. G. (2006) PTPN11 (Shp2) mutations in LEOPARD syndrome have dominant Negative, not activating, effects. *J. Biol. Chem.* **281**, 6785–6792
9. Mainardi, S., Mulero-Sánchez, A., Prahallad, A., Germano, G., Bosma, A., Krimpenfort, P., Lieftink, C., Steinberg, J. D., de Wit, N., Gonçalves-Ribeiro, S., Nadal, E., Bardelli, A., Villanueva, A., and Bernards, R. (2018) SHP2 is required for growth of KRAS-mutant non-small-cell lung cancer in vivo. *Nat. Med.* **24**, 961–967
10. Ruess, D. A., Heynen, G. J., Ciecielski, K. J., Ai, J., Berninger, A., Kabacaoglu, D., Görgülü, K., Dantes, Z., Wörmann, S. M., Diakopoulos, K. N., Karpathaki, A. F., Kowalska, M., Kaya-Aksoy, E., Song, L., van der Laan, E. A. Z., *et al.* (2018) Mutant KRAS-driven cancers depend on PTPN11/SHP2 phosphatase. *Nat. Med.* **24**, 954–960
11. Higashi, H., Tsutsumi, R., Muto, S., Sugiyama, T., Azuma, T., Asaka, M., and Hatakeyama, M. (2002) SHP-2 tyrosine phosphatase as an Intracellular target of *Helicobacter pylori* CagA protein. *Science* **295**, 683–686

12. Hatakeyama, M. (2004) Oncogenic mechanisms of the Helicobacter pylori CagA protein. *Nat. Rev. Cancer* **4**, 688

13. Okazaki, T., Chikuma, S., Iwai, Y., Fagarasan, S., and Honjo, T. (2013) A rheostat for immune responses: The unique properties of PD-1 and their advantages for clinical application. *Nat. Immunol.* **14**, 1212

14. Gavrieli, M., Watanabe, N., Loftin, S. K., Murphy, T. L., and Murphy, K. M. (2003) Characterization of phosphotyrosine binding motifs in the cytoplasmic domain of B and T lymphocyte attenuator required for association with protein tyrosine phosphatases SHP-1 and SHP-2. *Biochem. Biophys. Res. Commun.* **312**, 1236–1243

15. Okazaki, T., Maeda, A., Nishimura, H., Kurosaki, T., and Honjo, T. (2001) PD-1 immunoreceptor inhibits B cell receptor-mediated signaling by recruiting src homology 2-domain-containing tyrosine phosphatase 2 to phosphotyrosine. *Proc. Natl. Acad. Sci.* **98**, 13866–13871

16. Chen, Y.-N. P., LaMarche, M. J., Chan, H. M., Fekkes, P., Garcia-Fortanet, J., Acker, M. G., Antonakos, B., Chen, C. H.-T., Chen, Z., Cooke, V. G., Dobson, J. R., Deng, Z., Fei, F., Firestone, B., Fodor, M., *et al.* (2016) Allosteric inhibition of SHP2 phosphatase inhibits cancers driven by receptor tyrosine kinases. *Nature* **535**, 148

17. Xie, J., Si, X., Gu, S., Wang, M., Shen, J., Li, H., Shen, J., Li, D., Fang, Y., Liu, C., and Zhu, J. (2017) Allosteric inhibitors of SHP2 with therapeutic potential for cancer Treatment. *J. Med. Chem.* **60**, 10205–10219

18. Liu, W., Yu, B., Xu, G., Xu, W.-R., Loh, M. L., Tang, L.-D., and Qu, C.-K. (2013) Identification of Cryptotanshinone as an inhibitor of oncogenic protein tyrosine phosphatase SHP2 (PTPN11). *J. Med. Chem.* **56**, 7212–7221

19. LaRochelle, J. R., Fodor, M., Ellegast, J. M., Liu, X., Vemulapalli, V., Mohseni, M., Stams, T., Buhrlage, S. J., Stegmaier, K., LaMarche, M. J., Acker, M. G., and Blacklow, S. C. (2017) Identification of an allosteric benzothiazolopyrimidone inhibitor of the oncogenic protein tyrosine phosphatase SHP2. *Bioorg. Med. Chem.* **25**, 6479–6485

20. LaRochelle, J. R., Fodor, M., Vemulapalli, V., Mohseni, M., Wang, P., Stams, T., LaMarche, M. J., Chopra, R., Acker, M. G., and Blacklow, S. C. (2018) Structural reorganization of SHP2 by oncogenic mutations and implications for oncoprotein resistance to allosteric inhibition. *Nat. Commun.* **9**, 4508

21. Barr, A. J., Ugochukwu, E., Lee, W. H., King, O. N. F., Filippakopoulos, P., Alfano, I., Savitsky, P., Burgess-Brown, N. A., Müller, S., and Knapp, S. (2009) Large-scale structural analysis of the Classical human protein tyrosine phosphatome. *Cell* **136**, 352–363

22. Pedersen, A. K., Peters, G. H., Moller, K. B., Iversen, L. F., and Kastrup, J. S. (2004) Water-molecule network and active-site flexibility of apo protein tyrosine phosphatase 1B. *Acta Crystallogr. Section D* **60**, 1527–1534

23. Whittier, S. K., Hengge, A. C., and Loria, J. P. (2013) Conformational motions regulate Phosphoryl transfer in related protein tyrosine phosphatases. *Science* **341**, 899–903

24. Brandão, T. A. S., Hengge, A. C., and Johnson, S. J. (2010) Insights into the reaction of protein-tyrosine phosphatase 1B: Crystal structures for transition state ANALOGS OF both catalytic STEPS. *J. Biol. Chem.* **285**, 15874–15883

25. Hof, P., Pluskey, S., Dhe-Paganon, S., Eck, M. J., and Shoelson, S. E. (1998) Crystal structure of the tyrosine phosphatase SHP-2. *Cell* **92**, 441–450

26. LaRochelle, J. R., Fodor, M., Xu, X., Durzynska, I., Fan, L., Stams, T., Chan, H. M., LaMarche, M. J., Chopra, R., Wang, P., Fortin, P. D., Acker, M. G., and Blacklow, C. S. (2016) Structural and functional Consequences of three cancer-associated mutations of the oncogenic phosphatase SHP2. *Biochemistry* **55**, 2269–2277

27. Yu, Z.-H., Xu, J., Walls, C. D., Chen, L., Zhang, S., Zhang, R., Wu, L., Wang, L., Liu, S., and Zhang, Z.-Y. (2013) Structural and Mechanistic insights into LEOPARD syndrome-associated SHP2 mutations. *J. Biol. Chem.* **288**, 10472–10482

28. Pádua, R. A. P., Sun, Y., Marko, I., Pitsawong, W., Stiller, J. B., Otten, R., and Kern, D. (2018) Mechanism of activating mutations and allosteric drug inhibition of the phosphatase SHP2. *Nat. Commun.* **9**, 4507

29. Lerner, E., Cordes, T., Ingargiola, A., Alhadid, Y., Chung, S. Y., Michalet, X., and Weiss, S. (2018) Toward dynamic structural biology: Two decades of single-molecule Förster resonance energy transfer. *Science* **359**, eaan1133

30. Craggs, T. D. (2017) Cool and dynamic: Single-molecule fluorescence-based structural biology. *Nat. Methods* **14**, 123

31. Roy, R., Hohng, S., and Ha, T. (2008) A practical guide to single-molecule FRET. *Nat. Methods* **5**, 507

32. Chin, J. W., Santoro, S. W., Martin, A. B., King, D. S., Wang, L., and Schultz, P. G. (2002) Addition of p-Azido-l-phenylalanine to the genetic code of Escherichia coli. *J. Am. Chem. Soc.* **124**, 9026–9027

33. Young, T. S., Ahmad, I., Yin, J. A., and Schultz, P. G. (2010) An enhanced system for unnatural amino acid Mutagenesis in E. coli. *J. Mol. Biol.* **395**, 361–374

34. Hong, V., Presolski, S. I., Ma, C., and Finn, M. G. (2009) Analysis and Optimization of Copper-Catalyzed Azide–alkyne Cycloaddition for Bioconjugation. *Angew. Chem. Int. Ed.* **48**, 9879–9883

35. Tyagi, S., and Lemke, E. A. (2013) Chapter 9 - Genetically encoded click Chemistry for single-molecule FRET of proteins. In Conn, P. M., ed., *Methods in Cell Biology* **113**. Elsevier Academic Press, San Diego, CA: 169–187

36. Chandradoss, S. D., Haagsma, A. C., Lee, Y. K., Hwang, J.-H., Nam, J.-M., and Joo, C. (2014) Surface passivation for single-molecule protein studies. *J. Vis. Exp.*, 50549

37. Chan, G., Kalaitzidis, D., and Neel, B. G. (2008) The tyrosine phosphatase Shp2 (PTPN11) in cancer. *Cancer Metastasis Rev.* **27**, 179–192

38. Marchi, M., and Ballone, P. (1999) Adiabatic bias molecular dynamics: A method to navigate the conformational space of complex molecular systems. *J. Chem. Phys.* **110**, 3697–3702

39. Paci, E., and Karplus, M. (1999) Forced unfolding of fibronectin type 3 modules: An analysis by biased molecular dynamics simulations. *J. Mol. Biol.* **288**, 441–459

40. Imhof, D., Wavreille, A.-S., May, A., Zacharias, M., Tridandapani, S., and Pei, D. (2006) Sequence Specificity of SHP-1 and SHP-2 src homology 2 domains: Critical ROLES OF residues beyond the pY+3 position. *J. Biol. Chem.* **281**, 20271–20282

41. Zhang, Y., Zhang, J., Yuan, C., Hard, R. L., Park, I.-H., Li, C., Bell, C., and Pei, D. (2011) Simultaneous binding of two Peptidyl Ligands by a src homology 2 domain. *Biochemistry* **50**, 7637–7646

42. Barford, D., and Neel, B. G. (1998) Revealing mechanisms for SH2 domain mediated regulation of the protein tyrosine phosphatase SHP-2. *Structure* **6**, 249–254

43. Hayashi, T., Senda, M., Suzuki, N., Nishikawa, H., Ben, C., Tang, C., Nagase, L., Inoue, K., Senda, T., and Hatakeyama, M. (2017) Differential mechanisms for SHP2 binding and activation are Exploited by Geographically distinct *Helicobacter pylori* CagA Oncoproteins. *Cell Rep.* **20**, 2876–2890

44. Welham, M. J., Dechert, U., Leslie, K. B., Jirik, F., and Schrader, J. W. (1994) Interleukin (IL)-3 and granulocyte/macrophage colony-stimulating factor, but not IL-4, induce tyrosine phosphorylation, activation, and association of SHPTP2 with Grb2 and phosphatidylinositol 3'-kinase. *J. Biol. Chem.* **269**, 23764–23768

45. Bone, H., Dechert, U., Jirik, F., Schrader, J. W., and Welham, M. J. (1997) SHP1 and SHP2 protein-tyrosine phosphatases associate with βc after Interleukin-3-induced receptor tyrosine phosphorylation: Identification OF potential binding sites and substrates. *J. Biol. Chem.* **272**, 14470–14476

46. Sugimoto, S., Wandless, T. J., Shoelson, S. E., Neel, B. G., and Walsh, C. T. (1994) Activation of the SH2-containing protein tyrosine phosphatase, SH-PTP2, by phosphotyrosine-containing peptides derived from insulin receptor substrate-1. *J. Biol. Chem.* **269**, 13614–13622

47. Pluskey, S., Wandless, T. J., Walsh, C. T., and Shoelson, S. E. (1995) Potent stimulation of SH-PTP2 phosphatase activity by simultaneous occupancy of both SH2 domains. *J. Biol. Chem.* **270**, 2897–2900

48. Lee, C.-H., Kominos, D., Jacques, S., Margolis, B., Schlessinger, J., Shoelson, S. E., and Kuriyan, J. (1994) Crystal structures of peptide complexes of the amino-terminal SH2 domain of the Syp tyrosine phosphatase. *Structure* **2**, 423–438

49. Zhang, Y., Ha, T., and Marqusee, S. (2018) Editorial Overview: Single-molecule Approaches up to Difficult Challenges in folding and dynamics. *J. Mol. Biol.* **430**, 405–408

50. Hatakeyama, M. (2017) Structure and function of *Helicobacter pylori* CagA, the first-identified bacterial protein involved in human cancer. *Proc. Jpn. Acad. Ser. B* **93**, 196–219

51. Siveen, K. S., Prabhu, K. S., Achkar, I. W., Kuttikrishnan, S., Shyam, S., Khan, A. Q., Merhi, M., Dermime, S., and Uddin, S. (2018) Role of non receptor tyrosine kinases in Hematological Malignances and its targeting by Natural products. *Mol. Cancer* **17**, 31

52. Liu, B. A., and Nash, P. D. (2012) Evolution of SH2 domains and phosphotyrosine signalling networks. *Philosophical Trans. R. Soc. Lond. Ser. B, Biol. Sci.* **367**, 2556–2573

53. Wang, W., Liu, L., Song, X., Mo, Y., Komma, C., Bellamy, H. D., Zhao, Z. J., and Zhou, G. W. (2011) Crystal structure of human protein tyrosine phosphatase SHP-1 in the open conformation. *J. Cell. Biochem.* **112**, 2062–2071

54. Mócsai, A., Ruland, J., and Tybulewicz, V. L. J. (2010) The SYK tyrosine kinase: A crucial player in diverse biological functions. *Nat. Rev. Immunol.* **10**, 387

55. Sada, K., Takano, T., Yanagi, S., and Yamamura, H. (2001) Structure and function of Syk protein-tyrosine Kinase1. *J. Biochem.* **130**, 177–186

56. Mellor, P., Furber Levi, A., Nyarko Jennifer, N. K., and Anderson Deborah, H. (2012) Multiple roles for the p85α isoform in the regulation and function of PI3K signalling and receptor trafficking. *Biochem. J.* **441**, 23–37

57. Miled, N., Yan, Y., Hon, W.-C., Perisic, O., Zvelebil, M., Inbar, Y., Schneidman-Duhovny, D., Wolfson, H. J., Backer, J. M., and Williams, R. L. (2007) Mechanism of two Classes of cancer mutations in the phosphoinositide 3-kinase catalytic Subunit. *Science* **317**, 239–242

58. Taniguchi, C. M., Emanuelli, B., and Kahn, C. R. (2006) Critical nodes in signalling pathways: Insights into insulin action. *Nat. Rev. Mol. Cell Biol.* **7**, 85

59. Pamonsinlapatham, P., Slimane, R. H., Lepelletier, Y., Allain, B., Toccafondi, M., Garbay, C., and Raynaud, F. (2009) P120-Ras GTPase activating protein (RasGAP): A multi-interacting protein in downstream signaling. *Biochimie* **91**, 320–328

60. Tocque, B., Delumeau, I., Parker, F., Maurier, F., Multon, M. C., and Schweighoffer, F. (1997) Ras-GTPase activating protein (GAP): A Putative effector for Ras. *Cell Signal.* **9**, 153–158